

A Case Study on the Far-Field Properties of Propagating Tropospheric Gravity Waves

CLAUDIA C. STEPHAN^a

*Department of Atmospheric and Oceanic Sciences, University of Colorado Boulder,
Boulder, Colorado*

M. JOAN ALEXANDER

NorthWest Research Associates, Inc., CoRA Office, Boulder, Colorado

MICHAEL HEDLIN AND CATHERINE D. DE GROOT-HEDLIN

*Laboratory for Atmospheric Acoustics, University of California, San Diego,
San Diego, California*

LARS HOFFMANN

Jülich Supercomputing Centre, Forschungszentrum Jülich, Jülich, Germany

(Manuscript received 6 February 2016, in final form 28 May 2016)

ABSTRACT

Mesoscale gravity waves were observed by barometers deployed as part of the USArray Transportable Array on 29 June 2011 near two mesoscale convective systems in the Great Plains region of the United States. Simultaneously, AIRS satellite data indicated stratospheric gravity waves propagating away from the location of active convection. Peak perturbation pressure values associated with waves propagating outside of regions where there was precipitation reached amplitudes close to 400 Pa at the surface. Here the origins of the waves and their relationship to observed precipitation are investigated with a specialized model study. Simulations with a 4-km resolution dry numerical model reproduce the propagation characteristics and amplitudes of the observed waves with a high degree of quantitative similarity despite the absence of any boundary layer processes, surface topography, or moist physics in the model. The model is forced with a three-dimensional, time-dependent latent heating/cooling field that mimics the latent heating inside the precipitation systems. The heating is derived from the network of weather radar precipitation observations. This shows that deep, intense latent heat release within the precipitation systems is the key forcing mechanism for the waves observed at ground level by the USArray. Furthermore, the model simulations allow for a more detailed investigation of the vertical structure and propagation characteristics of the waves. It is found that the stratospheric and tropospheric waves are triggered by the same sources, but have different spectral properties. Results also suggest that the propagating tropospheric waves may potentially remotely interact with and enhance active precipitation.

^a Current affiliation: National Centre for Atmospheric Science—Climate, Department of Meteorology, University of Reading, Reading, United Kingdom.

Corresponding author address: Claudia Stephan, Department of Meteorology, University of Reading, P.O. Box 243, Reading RG6 6BB, United Kingdom.
E-mail: c.c.stephan@reading.ac.uk

1. Introduction

The Earthscope USArray Transportable Array (TA) is a network of approximately 400 seismo-acoustic stations deployed on a 70-km Cartesian grid covering an area of 2 000 000 km² in the continental United States (Busby et al. 2006). The network moved eastward through station redeployments between 2004 and 2013, has since left the lower 48 states and is being redeployed

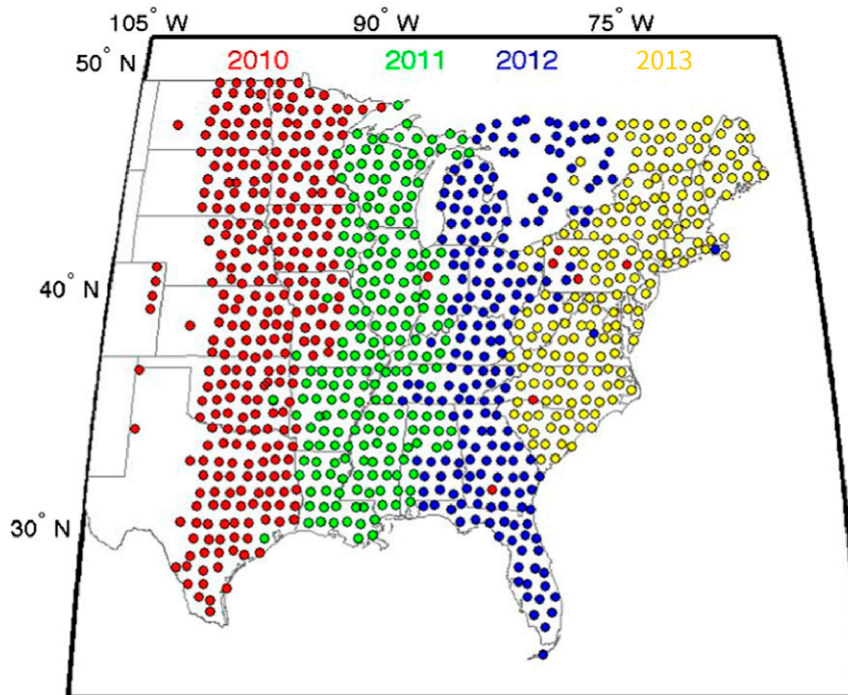


FIG. 1. Deployment history of operating Transportable Array stations equipped with Micro Electro-Mechanical System (MEMS) pressure sensors for the years 2010–13.

in Alaska. Although the array was originally designed for seismological studies, in 2009 an atmospheric sensor package was deployed at TA sites along with the seismic sensors, recording pressure variations at the earth's surface. Figure 1 shows the locations of operating stations equipped with these sensors for the years 2010–13.

Propagating signals in surface pressure surrounding severe precipitation systems have been observed with the TA, and were previously analyzed with a coherent detection method described by De Groot-Hedlin et al. (2014). Such large-amplitude surface pressure changes have previously been reported and connected to gravity waves (e.g., Koppel et al. 2000). The large number of TA sensors placed on a nearly regular Cartesian grid across a large region allows tracking of coherent signal propagation over long distances, and their method was designed to minimize spatial aliasing problems. The results showed that the typical 70-km spacing of the stations in the array permits the study of coherent signals with periods longer than ~ 40 min and wavelengths longer than ~ 40 km. These include a broad range of gravity waves with a wide range of propagation speeds. De Groot-Hedlin et al. (2014) showed that the largest amplitude waves also had the longest periods, and their analysis focused on signals in the 2–4-h band that displayed wavelengths longer than the interstation spacing.

Here we investigate the apparent relationship of the gravity wave surface pressure signals observed at ground level by the TA to severe precipitation systems. We use precipitation measurements from Next Generation Weather Radar (NEXRAD; OFCM 2006) weather radar stations and a specialized model, which has previously been shown to accurately simulate gravity waves in the far-field emanating from severe precipitation systems over the continental United States. We will consider a broader band of 1–8 h that includes most gravity waves that are well resolved by the array.

Our study is an investigation into the origins of the observed waves, their propagation and vertical structure, and their relationship to precipitation in a detailed case study. The selected case occurred during the night of 28–29 June 2011 over the central United States when the TA spanned 90° – 100° W longitudes over the Great Plains west of the Mississippi. The case, illustrated by radar mosaics in Fig. 2, includes two intense but relatively isolated precipitation systems: one over the northeastern corner of Texas on the evening of 28 June and a second over the Oklahoma Panhandle that intensified in the postmidnight hours of 29 June. These two precipitation systems occurred near the eastern and western edges of the TA, respectively, and the relatively isolated nature of the two precipitation systems makes this a good case for investigating the origins and remote

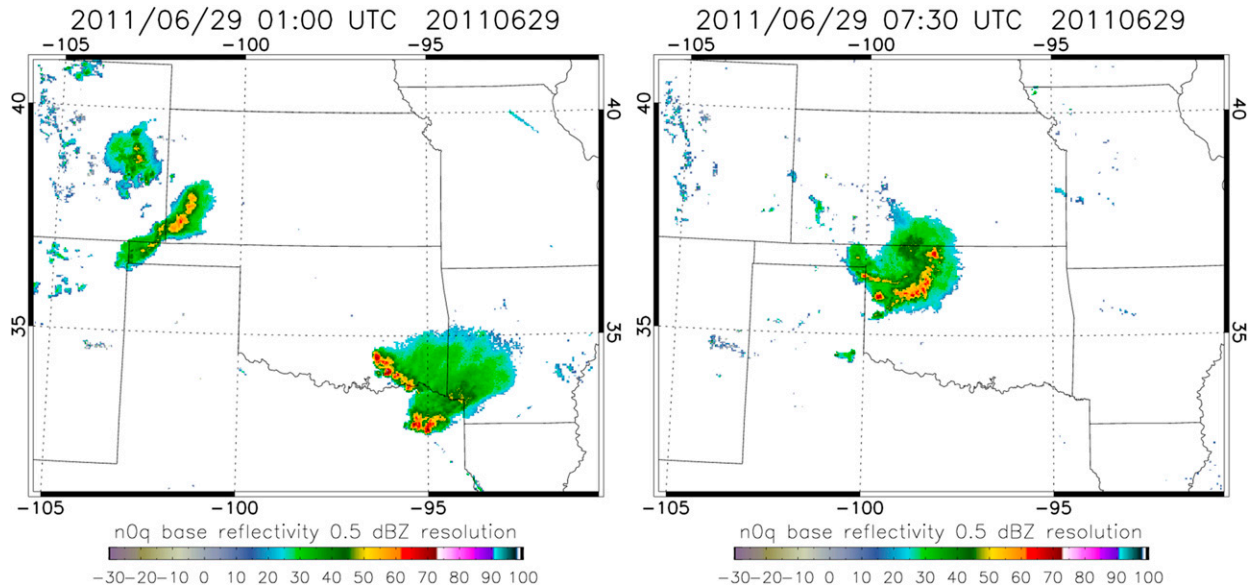


FIG. 2. Mosaics of radar reflectivity generated with NEXRAD data obtained from the Iowa State Environmental Mesonet Archive (<https://mesonet.agron.iastate.edu>). (Courtesy of D. Ahijevych.)

propagation of gravity waves observed in TA surface pressure measurements.

We use the modeling approach of Stephan and Alexander (2015) to simulate gravity waves forced by realistically varying convective latent heating and cooling in an idealized dry version of the Weather Research and Forecasting (WRF) Model (Skamarock et al. 2008). The heating/cooling field is three dimensional and time varying and derived directly from the NEXRAD-observed precipitation using an algorithm described in Stephan and Alexander (2015). The algorithm was trained on realistic simulations of severe precipitation systems with full-physics WRF hindcasts, but the use of the idealized model with radar precipitation in the present study permits direct comparisons to the spatial and temporal variations observed within the TA. Such direct comparisons are not possible in full-physics WRF hindcasts because the locations and timing of individual rain cells are never simulated accurately, yet these details are crucial for accurate simulation of the gravity wave responses.

With this method, we will investigate the horizontal and vertical propagation characteristics of the gravity wave field, the wave amplitudes, and relationship to precipitation. Previous studies have suggested a potential role for convectively generated gravity waves in the organization of convective rain clouds (e.g., Mapes 1993; Yang and Houze 1995; Tulich et al. 2007). The importance of gravity waves in triggering and interacting with new convective systems has previously been demonstrated in two-dimensional models (Tulich and Mapes

2008; Lane and Zhang 2011; Stechmann and Majda 2009) and studies of observed events (Ruppert and Bosart 2014; Koch and Siedlarz 1999). It has been suggested that gravity waves may initiate new convective cells in the far field (e.g., Shige and Satomura 2001; Fovell 2002).

While our dry model approach cannot directly investigate these feedbacks of gravity waves on precipitation, the model makes the normally invisible far-field gravity waves visible, permitting us to examine the realistically simulated gravity wave dynamics and their potential to influence low-level moisture convergence and precipitation. Our main goal, however, is to show that the new modeling approach can identify the sources of the waves observed by the high-density array of surface stations.

The paper is structured as follows: a summary of the weather situation during the time of this case study will be given in section 2a and the method and numerical model will be described in section 2b. We next examine the vertical structure of the simulated waves in section 2c and use linear theory to relate the shape of the heating profiles to the propagation characteristics of the waves. In section 3, we compare the wave patterns and amplitudes of simulated and observed waves to show that the model predicts the surface measurements with good accuracy outside of regions where there was precipitation. We further show that satellite observations of waves in the stratosphere above the precipitation systems are consistent with both the model predictions and observations at ground level. Section 4 examines the

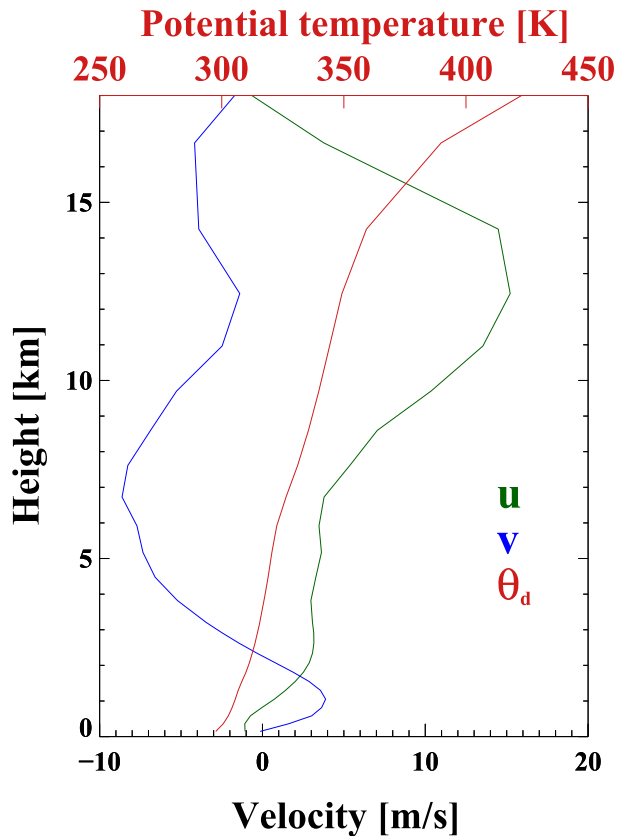


FIG. 4. Initialization profiles of potential temperature and horizontal winds computed from 24-h mean MERRA profiles. MERRA grid points inside the black dashed box shown in Fig. 3 were averaged.

24 km (30 hPa) with the upper 5 km consisting of a damping layer that was previously shown to prevent unphysical wave reflection at the upper boundary (Stephan and Alexander 2014).

Figure 5 shows simulated pressure perturbations at 500 m above the surface at 0200, 0600, and 1000 UTC. Red colors mark rain cells that exceed the convective threshold of $1 \text{ mm (10 min)}^{-1}$ (i.e., regions where the heating field in the idealized model is nonzero). At 0200 UTC both of the precipitation centers in the left panel of Fig. 2 are visible.

Different physical processes at different spatial scales are occurring simultaneously in the simulation. Recall that the model is initialized with a horizontally uniform profile of winds and potential temperature. In all three panels we observe that the slower time-scale components of the diabatic convective heating input to the model modify the thermal structure and larger-scale wind environment within the domain through potential vorticity changes. In the 0200 UTC panel the signature of this modification is characterized by mostly positive pressure perturbations in the northwest corner of the domain and mostly negative pressure perturbations in the southeast corner of the domain. The initially horizontally uniform background develops into a more complex state that resembles the actual environment surrounding deep convection. This adjustment to more realistic conditions is one reason why the modeling approach is successful in capturing the observed waves. The three panels of Fig. 5 show that waves are propagating both east- and westward. At any given time and location the local conditions, which are a combination of the initialization profile, mesoscale adjustments and wave interference, make certain directions more preferable.

The precipitation system centered at $\sim 95^\circ\text{W}$ is triggering strong westward-propagating pressure waves with peak-to-peak amplitudes on the order of 300 Pa. A negative perturbation pressure wave is followed by a

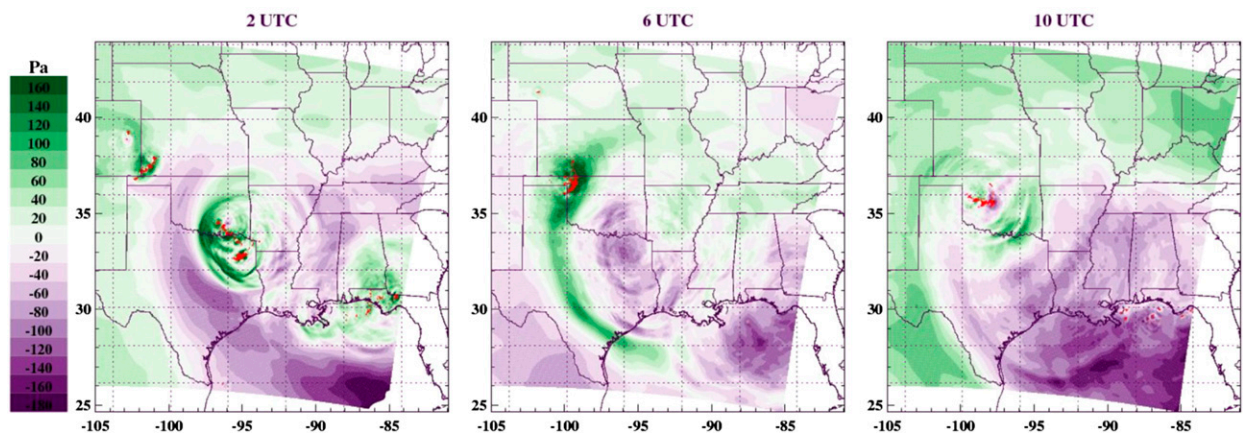


FIG. 5. Maps of simulated perturbation pressure, defined as the deviation from the domain mean pressure at each time, at 500-m altitude. Red areas mark regions that exceed the convective threshold of $1 \text{ mm (10 min)}^{-1}$ (i.e., regions where a heating/cooling field is turned on in the simulation).

more slowly moving positive wave. The positive perturbation pressure wave reaches the other precipitation system located at $\sim 100^\circ\text{W}$ around 0530 UTC. This second precipitation system is also triggering waves, which are clearly visible at the surface at 1000 UTC.

From these maps and Fig. 2 it is apparent that most of the precipitation, and therefore waves, in the model domain and the surrounding region of the United States are associated with the two well-confined precipitation systems. However, at 0200 and 1000 UTC some isolated cells exist in the southeast corner of the model domain (Fig. 5). While these wave-generating cells are included in the model, other cells that lie outside of the model domain are not. When comparing to observations in section 3 it should be taken into account that waves can propagate long distances and that some of the wave signals in the observations may be attributed to sources that lie outside of the simulated area.

c. Wave vertical structure and propagation characteristics

As mentioned in section 1, the TA is a very useful observational network for studying the occurrence frequencies and horizontal propagation characteristics of gravity waves at the surface. The WRF simulation in addition is able to reveal the vertical structure of these waves, which is required for explaining their propagation characteristics and for assessing the impact such waves may have on the atmosphere hundreds of kilometers away from their origin.

Figure 6 is a zonal cross section at 34°N and 0040 UTC showing the vertical structure of small-scale propagating waves to the west of an active center of convection. The line to the left of each panel shows the shape of the mean heating/cooling profile inside the convective region as derived by the heating algorithm from observed precipitation, and the thin black line marks a value of zero. From the top panel of Fig. 6, which shows vertical velocity, we observe that the dominant vertical wavelength of the waves in the troposphere corresponds to twice the depth of the heating. Also evident are waves propagating into the stratosphere with shorter vertical scales. For hydrostatic and nonrotational gravity waves, the group velocity vector is along lines of constant phase and the ratio of the intrinsic vertical group velocity to the horizontal group velocity can be expressed as

$$|\hat{c}_{gz}/\hat{c}_{gh}| = |k_h/m| = \left| k_h \frac{\hat{c}_h}{N_{\text{BV}}} \right| = \left| \frac{\hat{\omega}}{N_{\text{BV}}} \right|, \quad (1)$$

where k_h is the horizontal wavenumber, \hat{c}_h the intrinsic horizontal phase speed, m the vertical wavenumber, and

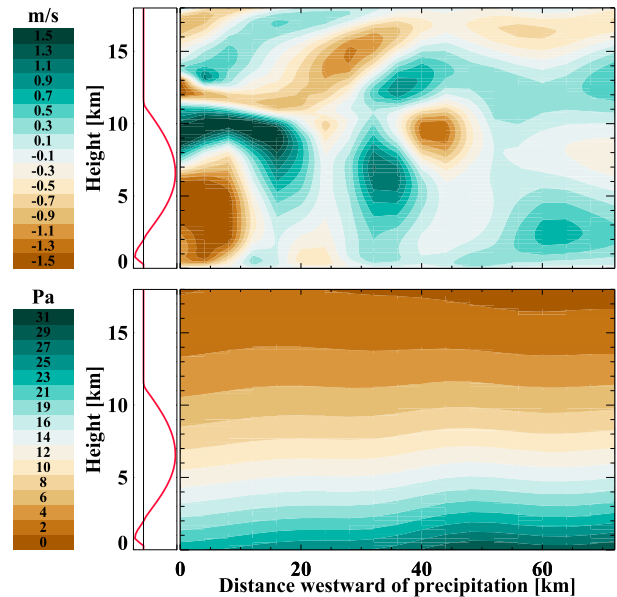


FIG. 6. Zonal cross sections of (top) vertical velocities and (bottom) perturbation pressure at 34°N and 0040 UTC to the west of active convection. The origin of the x axis is located at 96.2°W . The color scale for the top panel is saturated at $\pm 1.5 \text{ m s}^{-1}$ to emphasize the far-field waves, but vertical velocity values close to the heat source range from -2.3 to $+3.0 \text{ m s}^{-1}$. The shape of the mean heating/cooling profile inside the convective region is shown to the left of each panel.

$\hat{\omega}$ the intrinsic frequency (Fritts and Alexander 2003). Since this quantity is inversely proportional to the buoyancy frequency N_{BV} , which in the stratosphere has approximately double its tropospheric value, waves get refracted to shorter vertical wavelength as they cross the tropopause, as evident in Fig. 6.

The bottom panel of Fig. 6 shows the corresponding perturbation pressure. Note that the anomalies are all positive because of the focus here on a small region that lies within the positive phase of the larger-scale wave described in Fig. 5. Amplitudes are largest at the surface and decay linearly with altitude. In reality the earth's surface in the area of interest is not flat but its elevation varies between 0.0 and 1.2 km above sea level. Given that the large-scale variations in pressure are on the order of several hundred pascals (see Fig. 5) we will neglect topography when comparing to the surface observations in section 3, and focus on the model level at 500 m.

The vertical structure of the vertical velocity field displays some complexity. From linear theory it is expected that several wave modes are generated by the typical heating profiles in the model. It has been demonstrated that linear theory is successful in predicting the general shape of gravity wave spectra generated by a diabatic source in numerical simulations (Pandya and

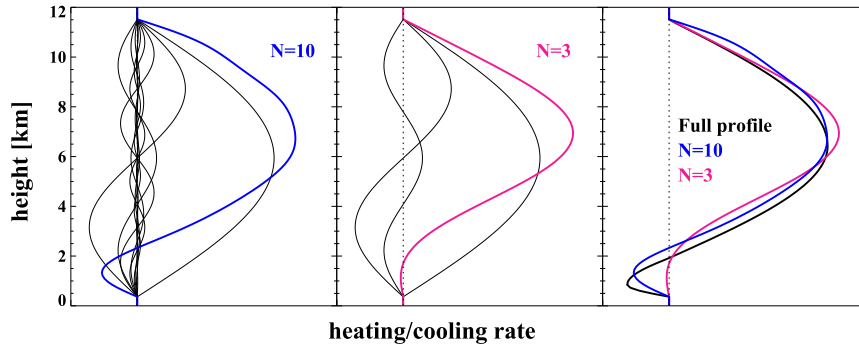


FIG. 7. Decomposition of the heating profile associated with the 99th percentile rain rate. (right) The full heating profile is shown (thick black line). The sums of the (left) first 10 and (middle) first 3 Fourier components are indicated by the colored lines. For details on the computation, please refer to the text.

Alexander 1999; Song et al. 2003). Figure 7 shows the decomposition of a heating profile $H(z)$ associated with a strong rain rate (thick black line in the right panel) into its first 10 (left panel) and first 3 (middle panel) Fourier components. The decomposition is given by

$$H(z) = \sum_{n=1}^{n=N} A_n \sin \frac{\pi n z}{D}. \quad (2)$$

Here, $D \approx 11$ km denotes the depth of the heating, which we define as the vertical distance between the bottom of the cooling layer and the top of the heating region. The Fourier decomposition consists of sine modes that meet the boundary conditions of vanishing amplitudes at the top and bottom of the vertical profile. This same analysis technique has previously been used in Alexander and Holton (2004) for interpreting far-field wave properties. The heating profile $H(z)$ is computed for a rain rate of $14 \text{ mm } (10 \text{ min})^{-1}$, which corresponds to the 99th percentile of $4 \text{ km} \times 4 \text{ km}$ 10-min rain rates seen in this study. The colored lines in Fig. 7 are the respective sums of the individual modes and are also shown in the right panel for comparison with the original profile.

As has been shown in Nicholls et al. (1991), linear theory predicts that the horizontal phase speed for a pure sine mode is given by

$$c_h = \frac{D}{n} \frac{N_{\text{BV}}}{\pi}. \quad (3)$$

The mean buoyancy frequency $N_{\text{BV}} = 0.012 \text{ s}^{-1}$ in the heating/cooling region is computed from the initialization profile of dry potential temperature shown in Fig. 4.

Table 1 shows the theoretical phase speed and explained variance for the first 10 Fourier modes. In

deriving a vertical heating/cooling profile from rain rates, all parameters of the profile $H(z)$ (bottom/top of the heating/cooling layers, heating/cooling amplitudes, and the levels at which these extrema are met) are linear functions of the rain rate. Therefore, choosing a different rain rate for computing $H(z)$ will make a difference to the phase speeds and the contribution of individual modes. However, for a 50% smaller rain rate phase speeds remain within 5% of those shown in Table 1. Therefore, a comparison between the single theoretical spectrum of Table 1 and the simulated spectrum can be made.

Figure 8 shows normalized absolute momentum flux spectra, given by

$$F(\kappa, \omega) = \sqrt{(uw^*)^2 + (vw^*)^2} \quad (4)$$

at 3 km (left panel) and 17 km (right panel) as a function of wavenumber and frequency. These spectra are computed from perturbation wind velocities using a three-dimensional Fourier analysis. Details of the computation are described in Stephan and Alexander (2014). Lines of constant phase speed labeled in units of meters per second are shown in white. Prominent lobes appear near the predicted top four ($n = 1, 2, 3, 4$) mode speeds of 40, 20, 15, and 10 m s^{-1} . The $n = 1$ mode is more pronounced in the stratosphere at 17 km compared to the 3-km level and the slowest $n > 5$ modes are more prominent in the troposphere. Equation (1) predicts that for a given horizontal wavenumber k_h waves with larger horizontal phase speeds \hat{c}_h escape into the stratosphere more quickly. This is consistent with the relatively larger abundance of slow (fast) waves in the troposphere (stratosphere). Deviations from the theoretical spectrum are expected for two reasons. As mentioned above, we assumed one specific rain rate for calculating the

TABLE 1. Theoretical phase speeds c , from Eq. (3), and percentage of explained variance, for the first 10 Fourier modes. Please refer to the text for further explanation.

n	c (m s^{-1})	Explained variance (%)
1	42.6	61.0
2	21.3	18.8
3	14.2	13.1
4	10.6	2.8
5	8.5	2.4
6	7.1	0.7
7	6.1	0.6
8	5.3	0.2
9	4.7	<0.1
10	4.3	<0.1

numbers in Table 1. Given that a wide variety of rain rates exist in the 24-h simulation, the simulated spectrum becomes blurred and continuous in wavenumber–frequency space. Second, the Fourier analysis is based on 24 h. This is enough time for waves, especially the fast waves of the $n = 1$ mode, to leave the domain and explains why the $n = 1$ mode is not as prominent in Fig. 8 as one might expect from its contribution (Table 1).

3. Comparisons with observations

This study uses data from barometric pressure sensors in the atmospheric sensor package deployed at each site of the TA. These instruments measure ambient pressure with an accuracy of 0.2 Pa, with the data digitized at 1 Hz. For further details see De Groot-Hedlin et al. (2014).

Figure 9 shows model perturbation pressure in units of pascals sampled at locations of TA installations and the corresponding TA recorded observations at 2-h intervals. A 1–8-h bandpass filter has been applied to both datasets. Time stamps in UTC are embedded in each panel. Comparing to Fig. 5 at 0200 UTC, we recognize the prominent negative perturbation wave that is followed by a strong positive perturbation. There is good agreement between the simulation and observations in terms of amplitude, location, and wavelength of this pattern. We see the waves propagating westward at later times and leaving the region of the TA. In the 0600 UTC panel a positive perturbation located above the Oklahoma Panhandle precipitation system starts near 37°N at the western side of the TA region and then propagates southeastward. There is again good agreement in amplitude and size of this feature between model and observations. At 1200 UTC precipitation and wave activity have mostly calmed down, but pressure perturbations on the order of 30 Pa remain. The model predicts the spatial extent and magnitudes of these residual perturbations very well. Disagreement, particularly in the southeast, may be attributed to additional convection to the east of the domain that may generate waves that were not captured by the simulation.

To better see the realistic representation of the timing, speed and amplitudes of the waves in the model, Fig. 10 shows time series from the simulations (Fig. 10a) and TA data (Fig. 10b). The TA data have been de-meaned

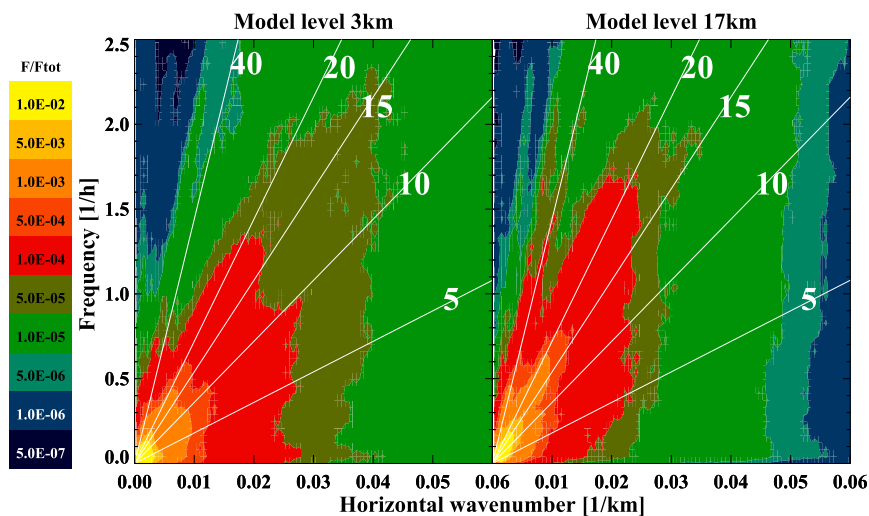


FIG. 8. Normalized absolute momentum flux spectra at (left) 3 and (right) 17 km as a function of horizontal wavenumber and frequency. A three-dimensional Fourier analysis was applied to obtain each spectrum as a function of frequency, zonal wavenumber k , and meridional wavenumber l . The horizontal wavenumber, shown on the x axis, is given by $\sqrt{(k^2 + l^2)}$ and is independent of the direction of wave propagation. Lines of constant phase speed in units of m s^{-1} are shown in white.

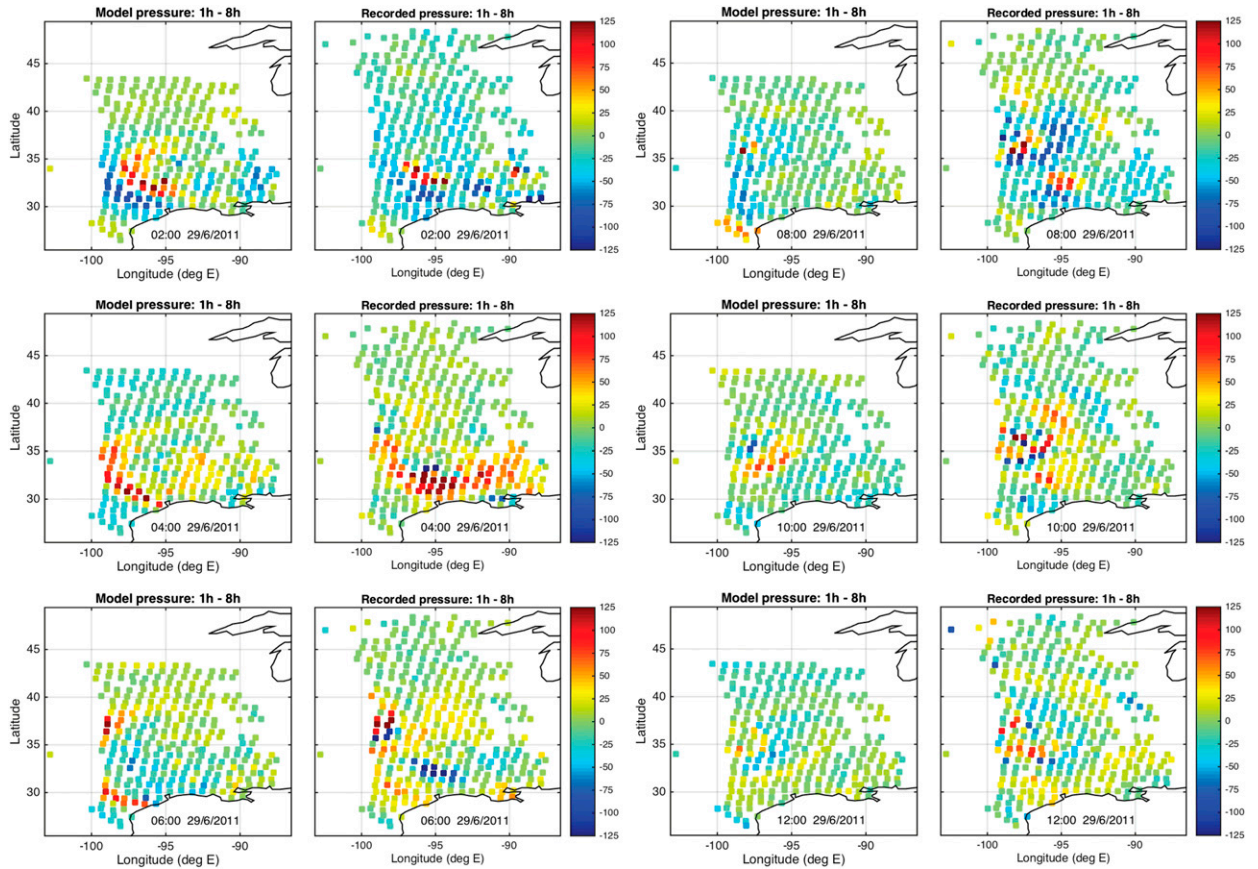


FIG. 9. Model perturbation pressure in units of Pa sampled at locations of TA installations and the corresponding TA recorded observations at 2-h intervals. A 1–8-h bandpass filter has been applied to both datasets. Time in UTC is shown at the bottom inside each panel.

and bandpass filtered from 1 to 8 h and the model domain-mean pressure has been subtracted from the simulated data at each time. All lines are normalized such that 1° in longitude corresponds to a pressure perturbation of 300 Pa. There are several differences in the details of the waves but the overall agreement between model and observations for the most intense wave trains is good. Red colors mark regions where rain exceeds $1 \text{ mm } (10 \text{ min})^{-1}$. To point out some similarities, in the $30^\circ\text{--}31^\circ\text{N}$ panel, both model and observations show westward-propagating waves during the time interval $\sim 0400\text{--}1200$ UTC. In the $32^\circ\text{--}33^\circ\text{N}$ panel, there are east- and westward-propagating waves that originate from a region with precipitation around $0600\text{--}0800$ UTC. Eastward-propagating waves are triggered in both the $36^\circ\text{--}37^\circ$ and $37^\circ\text{--}38^\circ\text{N}$ panels, and they dissipate after traveling for about the same amount of time and distance in both observed and modeled data. However, focusing on the red regions, which indicate precipitation, there is evidence from this comparison that perturbations may be underestimated in the model in regions where there was precipitation.

Figure 11 compares the simulated (solid histograms) and observed (dashed histograms) absolute perturbation pressure amplitudes of Fig. 10 close to convective regions (red) and to areas in the far-field (blue), defined here as regions that are separated by at least 0.75° of latitude/longitude from locations where rain rates greater than $1 \text{ mm } (10 \text{ min})^{-1}$ are observed. Data are normalized by the total number of grid points in the far field and grid points in the vicinity of convection, respectively. The relative occurrence frequency of large perturbation pressure amplitudes is much greater for regions in the vicinity of convection, even though substantial amplitudes greater than 200 Pa are reached in the observed far-field wave field. The potential for these waves to interact with or trigger remote convection will be discussed further in section 4. Furthermore we see that the model underestimates the amplitudes of waves in regions where there was precipitation, which we label as convectively coupled waves. We hypothesize that this difference between model and observation is due to the fact that the model does not include moist processes (e.g., mesoscale updrafts and downdrafts, cold pools,

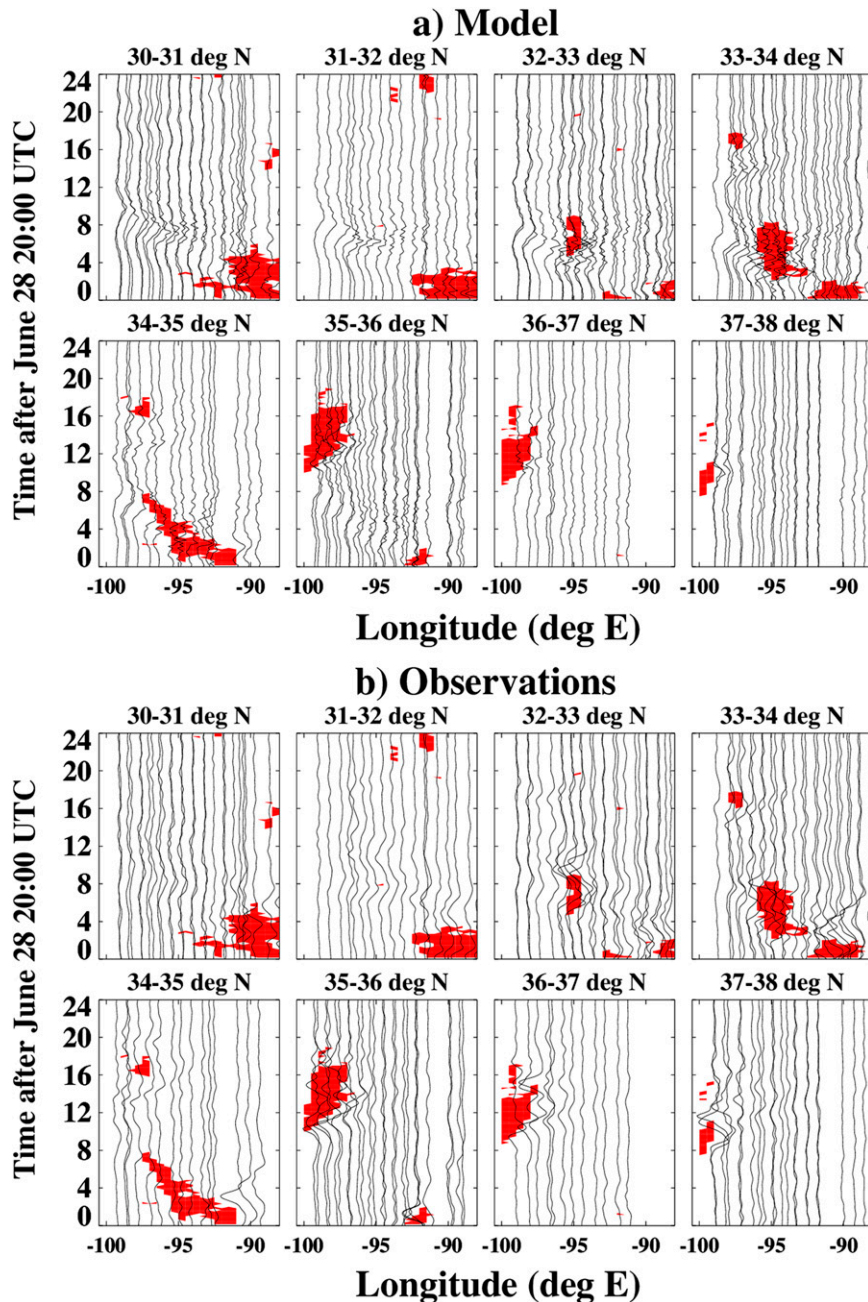


FIG. 10. Times series of model predictions and recorded data at locations of stations in the TA. (a) All model predictions in a set of 8 sections and (b) observations are shown. Each panel contains recordings (or model predictions) from all stations that were located in a narrow east–west corridor, with the latitude limits given in the figure captions, and with the zero-anomaly location of each trace along the x axis being determined by the stations longitude. Amplitudes are normalized such that 300 Pa correspond to 1° of longitude. The observed time series were bandpass filtered from 1 to 8 h. For simulated data the domain-mean pressure at each time has been removed. Regions of active convection are marked in red [rain rates exceeding a threshold of $1 \text{ mm (10 min)}^{-1}$].

and condensate mass). For instance, [Bacmeister et al. \(2012\)](#) show that the mass of condensate in convective clouds can significantly influence surface pressure, leading to corrections on the order of ~ 100 Pa.

The vertical velocity field in [Fig. 6](#) and the momentum flux spectrum at 17 km in [Fig. 8](#) indicate that some of the wave energy also propagates upward into the stratosphere. The Atmospheric Infrared Sounder (AIRS) on

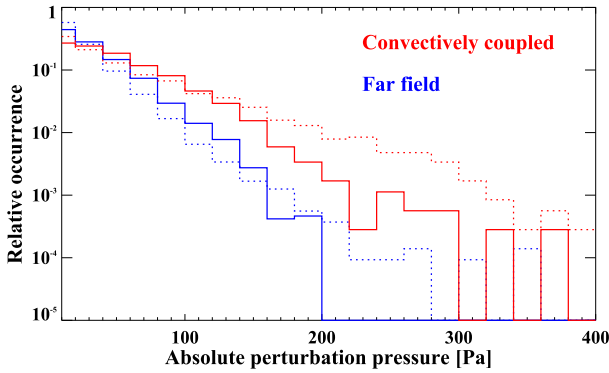


FIG. 11. Simulated absolute perturbation pressure amplitudes in the vicinity of precipitating regions (red), defined as areas separated by less than 0.75° of latitude/longitude from locations where rain rates greater than 1 mm (10 min)⁻¹ are observed and far-field areas (blue). Simulated data are shown as solid histograms and observed data are shown as dashed histograms. All data are normalized by the total number of grid points that lie in the far field and in the vicinity of convection, respectively.

board NASA’s *Aqua* satellite is a hyperspectral imager, and can observe gravity wave signals in the stratosphere at 4.3 μm as well as cloud-top brightness temperatures at 8.1 μm (Hoffmann and Alexander 2010; AIRS Science Team/Moustafa Chahine 2007). Low 8.1-μm brightness temperatures observed by AIRS when the satellite passed over 36°N, 98°W at 0805 UTC 29 June indicate a mesoscale convective system with convection overshooting the tropopause (left panel of Fig. 12). This precipitation system is seen in the right panel of Fig. 2. Simultaneous 4.3-μm brightness temperature perturbations indicate stratospheric gravity waves propagating to the east from this location.

Eastward-propagating waves were seen at the surface as well, see Fig. 5 at 1000 UTC and the 35°–36°N panel of Fig. 10. Figure 13 is a zonal cross section at 0700 UTC at 35.5°N, showing the simulated vertical velocity field in shades of gray and the heating/cooling region in purple. It shows the deep tropospheric waves that can be seen at the surface and waves propagating eastward into the stratosphere that are seen by the satellite.

4. Potential wave impacts on convection

In the previous sections we have seen that the model is capable of producing realistic gravity waves in the troposphere and above. Unlike surface or satellite observations the simulations contain information about the vertical structure of these waves and give us a more complete picture of their properties. In the case selected for this study, gravity waves triggered by one precipitation system encounter convection that is separated by several hundreds of kilometers. In this section we will examine whether the gravity waves may potentially play a role in strengthening the second precipitation system.

Figure 14 displays hourly maps of vertical displacement at 850 hPa calculated as

$$\Delta z = -\Delta\theta \left(\frac{\partial\theta}{\partial z} \right)^{-1}, \tag{5}$$

where Δθ is the potential temperature perturbation at 850 hPa and ∂θ/∂z is the vertical gradient of potential temperature, obtained from the initialization profile Fig. 4. Each panel shows the 2000 km × 2000 km WRF

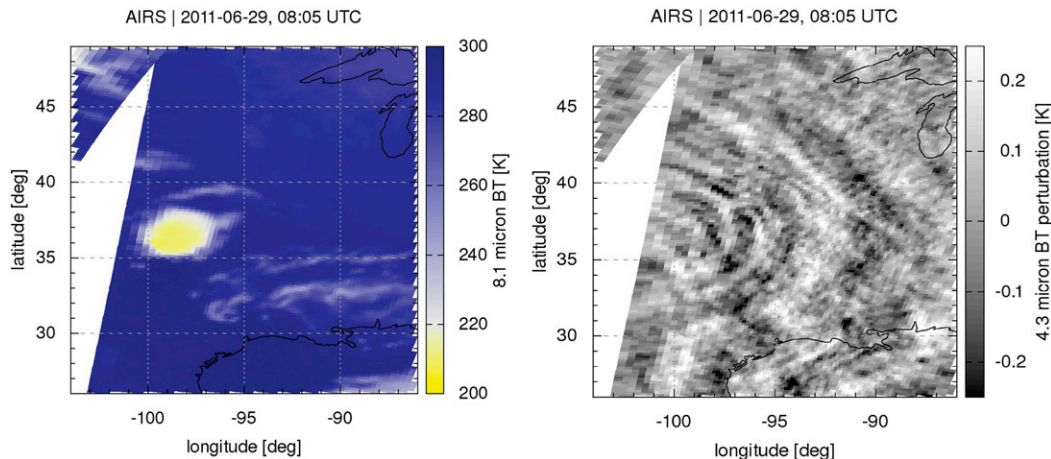


FIG. 12. (left) The 8.1- and (right) 4.3-μm brightness temperature perturbations observed by AIRS at 0805 UTC 29 Jun indicate a mesoscale convective system with convection overshooting the tropopause and eastward-propagating gravity waves, respectively. The images are computed using the method described in Hoffmann and Alexander (2010).

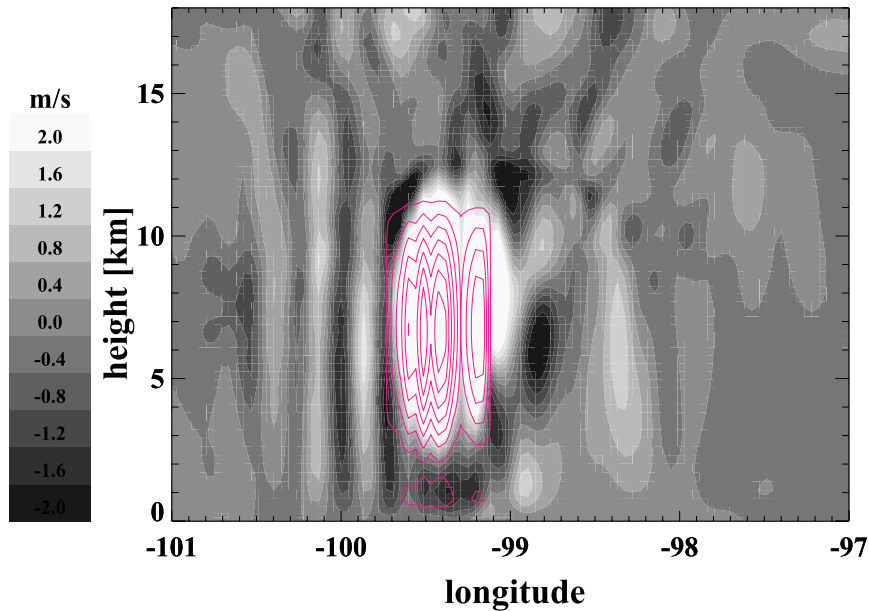


FIG. 13. Zonal cross section at 0700 UTC at 35.5°N, showing simulated vertical velocities (shades of gray) and the heating/cooling region (purple) at contour intervals of 0.003 K s⁻¹.

Model domain, and time (in UTC) is given in the bottom left of each panel. Regions with precipitation as determined by the radar observations are again marked in red. The blue box encloses the Oklahoma Panhandle

precipitation system and numbers above each box show the accumulated hourly areal mean precipitation in millimeters for the area of the box. To better resolve the temporal evolution of precipitation inside the box

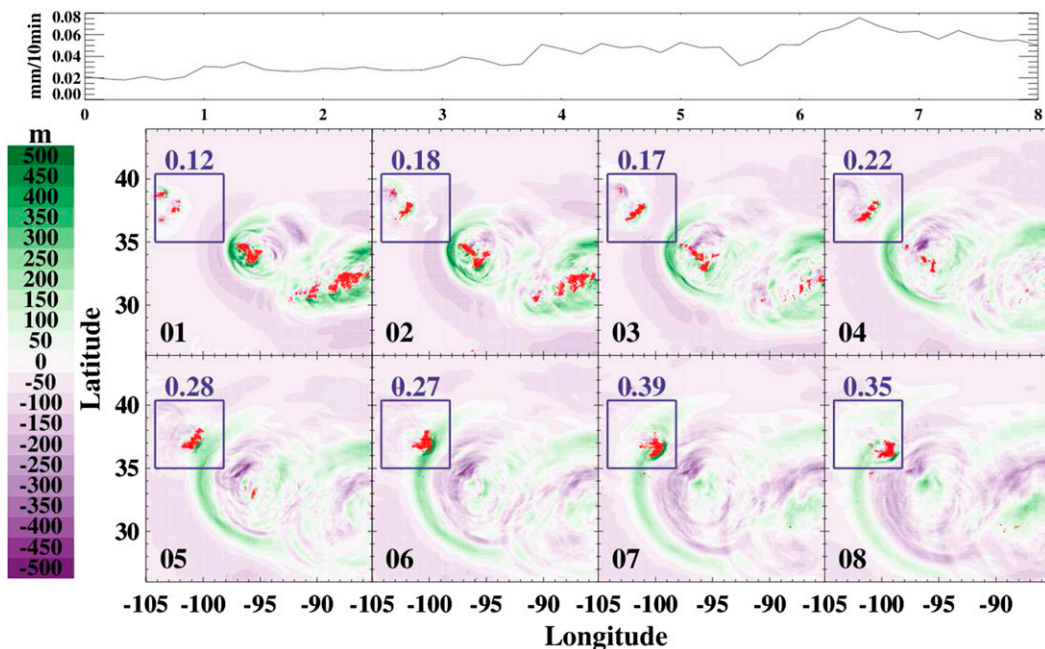


FIG. 14. Hourly maps of vertical displacement at 850 hPa computed from simulated potential temperature perturbations. Time in hours UTC is indicated in the bottom left of each panel. Red areas mark active convection [rain rates exceeding 1 mm (10 min)⁻¹ for some time during the hour]. The areal-mean precipitation rate in mm h⁻¹ inside the small blue box in each panel is shown above the box. The graph at the top of the figure shows the temporal evolution of areal-mean 10-min precipitation inside this small blue box between 0000 and 0800 UTC.

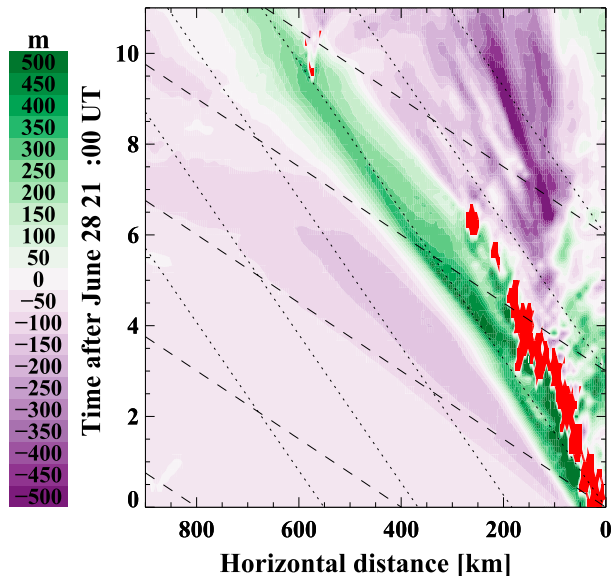


FIG. 15. Hovmöller diagram of 850-hPa vertical displacement at 34°N showing the region $104.1^{\circ}\text{--}94.4^{\circ}\text{W}$. Black dashed (dotted) lines mark constant propagation speeds of 40 (20) m s^{-1} relative to the mean zonal wind of 3 m s^{-1} in the heating region. Regions with precipitation are shown in red [rain rates exceeding $1 \text{ mm (10 min)}^{-1}$].

the plot at the top of Fig. 14 shows the corresponding mean 10-min rain rates between 0000 and 0800 UTC.

We observe a westward-propagating wave consisting of a widespread area with negative displacement followed by a well-defined positive displacement. These waves are triggered by the precipitation system located in the center of the domain at 0100 UTC and their signature was also apparent in the pressure perturbations shown in Fig. 5. An approximate doubling of the precipitation rate occurs as the positive phase of the propagating wave encounters the precipitation system active inside the box. This information is insufficient to establish a causal relationship between the wave and the strengthening of the precipitation system but it is consistent with the hypothesis that the gravity wave vertical displacements on the order of several hundred meters may alternately interfere with active convection and enhance it. There are many more factors that may influence the life cycle of this system, like changes in the background atmosphere that the idealized model cannot capture or the natural life cycle of the system.

Figure 15 is a Hovmöller diagram of vertical displacement at 34°N showing the region $104.1^{\circ}\text{--}94.4^{\circ}\text{W}$. The latitude of 34°N was chosen because it corresponds to the part of the circular wave train that is propagating to the west without much of a north- or southward component. This allows determination of the propagation speed when plotting against distance at a constant latitude. Precipitation is shown in red. The black dashed

(dotted) lines mark constant propagation speeds of 40 (20) m s^{-1} relative to the mean zonal wind of 3 m s^{-1} in the heating region. We can see that the negative displacement pressure wave has a faster propagation speed than the positive displacement wave. The positive wave travels at a velocity close to the $n = 2$ mode (see Table 1). The positive perturbation remains visible at the surface at distances far away from its origin, as opposed to the negative wave, which appears to be more dispersive. This is consistent with the horizontal maps shown in Fig. 14. The discussion in the last paragraph of section 2c suggests further that the negative displacement wave would propagate upward more quickly than the positive wave owing to its larger horizontal phase speed, which is proportional to the ratio of the vertical group velocity to the horizontal group velocity [Eq. (1)]. This effect may contribute to the more rapid attenuation of the negative displacement signal at the surface.

The linear response to gravity waves from a radially symmetric heating profile on isentropic displacements near the surface has been calculated in Mapes (1993). They assumed a heating profile consisting of two modes: one with a vertical wavelength of twice the depth of the heating ($n = 1$) and one with a wavelength equal to the depth of the heating ($n = 2$). In agreement with our nonlinear simulations and the TA observations they report that 3 h after a heating pulse, low-level isentropes are lifted at a distance of about 250 km from the heating while the faster-propagating $n = 1$ results in subsidence at distance of about 500 km [see Fig. 4b in Mapes (1993)]. The temporal and spatial scales seen here are consistent with the observational study by Lac et al. (2002), who found new convective cells appearing after a few hours and several hundred kilometers away from previous intense convection.

5. Summary and conclusions

In this case study we simulated gravity waves generated by latent heating in precipitation systems over the central United States. Model and observations show that these waves are associated with surface pressure signals that propagate distances longer than several hundred kilometers and commonly exceed amplitudes of 100 Pa. In our model, described previously in Stephan and Alexander (2015), waves are forced by a temporally and spatially varying heating/cooling field that is derived directly from radar-observed precipitation. This approach permits a direct comparison to surface pressure variations measured by barometers in the USArray Transportable Array and we find that wave amplitudes agree well outside of regions where there was precipitation. The model renders the three-dimensional far-field

wave structure visible, which normally is unknown because measurements tend to be limited to the surface or provide vertical information at individual points only.

We analyzed wave propagation characteristics across the full vertical extent of the troposphere and found that linear theory can successfully predict the propagation speed of the simulated waves from the shape of the vertical heating profiles. From Fig. 8, slower waves with speeds $<5 \text{ ms}^{-1}$ are relatively more prominent at the surface, and faster waves $>20 \text{ ms}^{-1}$ are relatively more prominent near the tropopause, which can be understood as a consequence of their respective slow and fast vertical group velocities. Waves with intermediate speeds of $5\text{--}20 \text{ ms}^{-1}$ are common at all levels. Similar wave signatures as those seen in the model were also observed in an overpass of the AIRS satellite instrument, indicating that waves measured at the surface and waves observed in the stratosphere are originating from common convective sources.

Vertical air parcel displacements at 850 hPa caused by waves propagating into regions that are far away from active convection exceed several hundred meters. In particular, we found evidence that the lifting phase of a 20 ms^{-1} propagating wave could be potentially responsible for an observed intensification of a separate developing precipitation system. The interaction of the propagating precipitation system with the convection occurred several hundred kilometers away from the origin of the wave and roughly 5 h after the wave was triggered. Our case study alone cannot provide enough evidence to prove that the intensification of precipitation is caused by the gravity wave, but it demonstrates that our method may be useful for future research. The modeling approach allows switching individual convective cells on or off, which can provide a clean way of disentangling coupled systems of waves and convection.

The approach, however, may not perform as well in other conditions. The case chosen for this study is particularly suitable for carrying out a comparison between simulated and observed waves because of well-defined, strong and isolated precipitation systems. Convection in the vicinity, but outside the model domain would generate additional waves that a simulation would miss and cause disagreement. Furthermore, the precipitation systems in this study developed within a region dominated by a broad ridge of high pressure. Relatively weak gradients in the horizontal profiles of pressure, wind, and temperature may contribute to a successful comparison. It is possible that our method of initializing the model with a horizontally uniform environment is not suitable for synoptic situations with strong gradients.

Acknowledgments. The authors thank the three anonymous reviewers for their constructive comments to improve the manuscript. We thank Dr. Stan Trier, Noah Brenowitz, and Professor Brian Mapes for insightful discussions. This work was supported by NSF Grant AGS-1318932 from the National Science Foundation programs in Physical and Dynamic Meteorology and Climate and Large-scale Dynamics and by NSF Award EAR-1358520. The Weather Research and Forecasting Model (<http://wrf-model.org/index.php>) is supported by the National Center for Atmospheric Research.

REFERENCES

- AIRS Science Team/Moustafa Chahine, 2007: AIRS/Aqua L1B Infrared (IR) geolocated and calibrated radiances V005, version 005. Goddard Earth Sciences Data and Information Services Center, Greenbelt, MD. [Available online at http://disc.gsfc.nasa.gov/datacollection/AIRIBRAD_005.html.]
- Alexander, M. J., and J. R. Holton, 2004: On the spectrum of vertically propagating gravity waves generated by a transient heat source. *Atmos. Chem. Phys.*, **4**, 923–932, doi:10.5194/acp-4-923-2004.
- Bacmeister, J. T., P. H. Lauritzen, A. Dai, and J. E. Truesdale, 2012: Assessing possible dynamical effects of condensate in high resolution climate simulations. *Geophys. Res. Lett.*, **39**, L04806, doi:10.1029/2011GL050533.
- Busby, R., F. Vernon, R. Newman, and L. Astiz, 2006: EarthScopes transportable array: Advancing eastward. *Eos, Trans. Amer. Geophys. Union*, **87** (Fall Meeting Supplement), Abstract U41B-0820.
- De Groot-Hedlin, C., M. Hedlin, and K. Walker, 2014: Detection of gravity waves across the USArray: A case study. *Earth Planet. Sci. Lett.*, **402**, 346–352, doi:10.1016/j.epsl.2013.06.042.
- Fovell, R. G., 2002: Upstream influence of numerically simulated squall-line storms. *Quart. J. Roy. Meteor. Soc.*, **128**, 893–912, doi:10.1256/0035900021643737.
- Fritts, D. C., and M. J. Alexander, 2003: Gravity wave dynamics and effects in the middle atmosphere. *Rev. Geophys.*, **41**, 1003, doi:10.1029/2001RG000106.
- Hoffmann, L., and M. J. Alexander, 2010: Occurrence frequency of convective gravity waves during the North American thunderstorm season. *J. Geophys. Res.*, **115**, D20111, doi:10.1029/2010JD014401.
- Koch, S. E., and L. M. Siedlarz, 1999: Mesoscale gravity waves and their environment in the central United States during STORM-FEST. *Mon. Wea. Rev.*, **127**, 2854–2879, doi:10.1175/1520-0493(1999)127<2854:MGWATE>2.0.CO;2.
- Koppel, L. L., L. F. Bosart, and D. Keyser, 2000: A 25-yr climatology of large-amplitude hourly surface pressure changes over the conterminous United States. *Mon. Wea. Rev.*, **128**, 51–68, doi:10.1175/1520-0493(2000)128<0051:AYCOLA>2.0.CO;2.
- Lac, C., J.-P. Lafore, and J.-L. Redelsperger, 2002: Role of gravity waves in triggering deep convection during TOGA COARE. *J. Atmos. Sci.*, **59**, 1293–1316, doi:10.1175/1520-0469(2002)059<1293:ROGWIT>2.0.CO;2.
- Lane, T. P., and F. Zhang, 2011: Coupling between gravity waves and tropical convection at mesoscales. *J. Atmos. Sci.*, **68**, 2582–2598, doi:10.1175/2011JAS3577.1.

- Mapes, B. E., 1993: Gregarious tropical convection. *J. Atmos. Sci.*, **50**, 2026–2037, doi:[10.1175/1520-0469\(1993\)050<2026:GTC>2.0.CO;2](https://doi.org/10.1175/1520-0469(1993)050<2026:GTC>2.0.CO;2).
- Nicholls, M. E., R. A. Pielke, and W. R. Cotton, 1991: Thermally forced gravity waves in an atmosphere at rest. *J. Atmos. Sci.*, **48**, 1869–1884, doi:[10.1175/1520-0469\(1991\)048<1869:TFGWIA>2.0.CO;2](https://doi.org/10.1175/1520-0469(1991)048<1869:TFGWIA>2.0.CO;2).
- OFCM, 2006: Federal meteorological handbook No. 11 (Part C). OFCM Tech. Rep. FCM-H11C-2006, 2-153–2-155.
- Pandya, R. E., and M. J. Alexander, 1999: Linear stratospheric gravity waves above convective thermal forcing. *J. Atmos. Sci.*, **56**, 2434–2446, doi:[10.1175/1520-0469\(1999\)056<2434:LSGWAC>2.0.CO;2](https://doi.org/10.1175/1520-0469(1999)056<2434:LSGWAC>2.0.CO;2).
- Rienecker, M. M., and Coauthors, 2011: MERRA: NASA's Modern-Era Retrospective Analysis for Research and Applications. *J. Climate*, **24**, 3624–3648, doi:[10.1175/JCLI-D-11-00015.1](https://doi.org/10.1175/JCLI-D-11-00015.1).
- Ruppert, J. H., and L. F. Bosart, 2014: A case study of the interaction of a mesoscale gravity wave with a mesoscale convective system. *Mon. Wea. Rev.*, **142**, 1403–1429, doi:[10.1175/MWR-D-13-00274.1](https://doi.org/10.1175/MWR-D-13-00274.1).
- Shige, S., and T. Satomura, 2001: Westward generation of eastward-moving tropical convective bands in TOGA COARE. *J. Atmos. Sci.*, **58**, 3724–3740, doi:[10.1175/1520-0469\(2001\)058<3724:WGOEMT>2.0.CO;2](https://doi.org/10.1175/1520-0469(2001)058<3724:WGOEMT>2.0.CO;2).
- Skamarock, W. C., and Coauthors, 2008: A description of the Advanced Research WRF version 3. NCAR Tech. Note NCAR/TN-475+STR, 113 pp., doi:[10.5065/D68S4MVH](https://doi.org/10.5065/D68S4MVH).
- Song, I.-S., H.-Y. Chun, and T. P. Lane, 2003: Generation mechanisms of convectively forced internal gravity waves and their propagation to the stratosphere. *J. Atmos. Sci.*, **60**, 1960–1980, doi:[10.1175/1520-0469\(2003\)060<1960:GMOCFI>2.0.CO;2](https://doi.org/10.1175/1520-0469(2003)060<1960:GMOCFI>2.0.CO;2).
- Stechmann, S. N., and A. J. Majda, 2009: Gravity waves in shear and implications for organized convection. *J. Atmos. Sci.*, **66**, 2579–2599, doi:[10.1175/2009JAS2976.1](https://doi.org/10.1175/2009JAS2976.1).
- Stephan, C. C., and M. J. Alexander, 2014: Summer season squall-line simulations: Sensitivity of gravity waves to physics parameterization and implications for their parameterization in global climate models. *J. Atmos. Sci.*, **71**, 3376–3391, doi:[10.1175/JAS-D-13-0380.1](https://doi.org/10.1175/JAS-D-13-0380.1).
- , and —, 2015: Realistic simulations of atmospheric gravity waves over the continental U.S. using precipitation radar data. *J. Adv. Model. Earth Syst.*, **7**, 823–835, doi:[10.1002/2014MS000396](https://doi.org/10.1002/2014MS000396).
- Tulich, S. N., and B. E. Mapes, 2008: Multiscale convective wave disturbances in the tropics: Insights from a two-dimensional cloud-resolving model. *J. Atmos. Sci.*, **65**, 140–155, doi:[10.1175/2007JAS2353.1](https://doi.org/10.1175/2007JAS2353.1).
- , D. A. Randall, and B. E. Mapes, 2007: Vertical-mode and cloud decomposition of large-scale convectively coupled gravity waves in a two-dimensional cloud-resolving model. *J. Atmos. Sci.*, **64**, 1210–1229, doi:[10.1175/JAS3884.1](https://doi.org/10.1175/JAS3884.1).
- Yang, M.-J., and R. A. Houze, 1995: Multicell squall-line structure as a manifestation of vertically trapped gravity waves. *Mon. Wea. Rev.*, **123**, 641–660, doi:[10.1175/1520-0493\(1995\)123<0641:MSLSAA>2.0.CO;2](https://doi.org/10.1175/1520-0493(1995)123<0641:MSLSAA>2.0.CO;2).